



Oxidation mechanism of W substituted Mo-Si-B alloys

Tuba Karahan^{a,1}, Gaoyuan Ouyang^{b,c,1}, Pratik K. Ray^{b,c,*}, M.J. Kramer^{b,c}, Mufit Akinc^{b,c}

^a Department of Metallurgical and Materials Engineering, Gedik University, Istanbul, Turkey

^b Department of Materials Science and Engineering, Iowa State University, Ames, IA, USA

^c Ames Laboratory, USDOE, Ames, IA, USA

ARTICLE INFO

Keywords:

Silicide
Transient oxidation
Glass
Silicate
Mo-Si-B

ABSTRACT

The oxidation mechanism of a $\text{Mo}_{55}\text{W}_{15}\text{Si}_{15}\text{B}_{15}$ alloy was established, and the effects of W content, oxidation temperature and microstructural length scale were determined. In addition to influencing the oxidation mechanism, the addition of W also destabilized the A15 phase which is consistent with our previous experiments in ternary Mo-W-Si alloys [1]. Microstructural investigation of the oxidized alloy revealed entrapped tungsten oxides at temperatures below 1300 °C, which volatilize above 1400–1500 °C. The presence of WO_3 in the oxide scale interrupts the surface coverage by the glassy borosilicate, thereby adversely affecting the oxidation behavior. In order to determine the effects of length scale, the microstructural evolution during the transient oxidation of cast and sintered alloys, with different microstructural length scales, was studied at 1100 and 1400 °C. Finer microstructure promoted faster borosilicate surface coverage at 1400 °C.

1. Introduction

Designing tough oxidation resistant refractory metal silicides is a key technological challenge that needs to be overcome in order to use these alloys for high temperature structural applications. High temperature oxidation behavior, mechanical properties and phase stability of Mo-Si-B based alloys have been extensively investigated over the last few decades [2–5]. However, no single alloy studied so far has demonstrated a combination of strength, toughness and oxidation resistance, which is essential for high temperature applications. This is a result of the conundrum posed by the Mo-Si-B ternary phase diagram. Alloys in the Mo-T2-A15 ($\text{Mo-Mo}_5\text{SiB}_2\text{-Mo}_3\text{Si}$) phase field show excellent fracture toughness [6] while alloys in the intermetallic rich regions show good oxidation resistance. Ideally, an alloy comprising of a Mo rich phase, the T1 phase and the T2 phase will offer a combination of excellent fracture toughness due to the Mo rich solid solution [7,8], creep resistance due to the presence of the T1 phase [9], and oxidation resistance due to the presence of B doped T1 [10] as well as the T2 [11] phases. The A15 phase, which lies between the metal rich solid solution and the T1 phase neither affords significant oxidation resistance [11], nor does it impart fracture toughness, as a result of only four active slip systems at room temperature [12]. Therefore, it was anticipated that the removal of the deleterious A15 phase will help in forming the desired three-phase microstructure consisting of Mo rich solid solution, the T1 phase and T2 phase.

The Mo_3Si (A15) phase can be destabilized with controlled alloying additions of Nb and W, as demonstrated by Ray et al. [1,13]. The addition of elements such as Nb and W results in the Fermi surface moving out of the pseudo-gap in the density of states, thereby creating an electronic structure instability [1]. Furthermore, a multi-phase assembly containing Nb or W is more stable than the single phase A15 structure [13,14]. While the experiments and theoretical calculations reported in the literature were carried out in ternary systems, without boron, it is expected that the addition of W will have a similar effect on the alloy phase assemblage even in the presence of boron due to its extremely low solubility in the A15 structure [15]. However, while the removal of the brittle A15 phase through W substitutions is expected to be beneficial for mechanical properties, the resulting effect on oxidation has not been established. W substitutions could increase the pecking range of the alloy at lower temperatures, resulting in poorer oxidation resistance at lower temperatures ($T < 1300$ °C). However, the removal of the A15 phase – which has poor oxidation resistance [11] – results in the formation of the T1 phase, which has better oxidation resistance [5]. This could conceivably improve the oxidation resistance above the pecking regime. Hence, it is important to investigate the oxidation behavior with W substitutions at different temperatures – in the pecking regime, as well as above the pecking regime.

The oxidation behavior of Nb modified Mo-Si-B and Nb-Si-B alloys have been extensively studied by a number of researchers [16–19]. Unlike Mo, which oxidizes to form a volatile MoO_3 , the oxidation of Nb

* Corresponding author. Department of Materials Science and Engineering, Iowa State University, Ames, IA, USA.

E-mail address: prat@iastate.edu (P.K. Ray).

¹ Equal first authors.

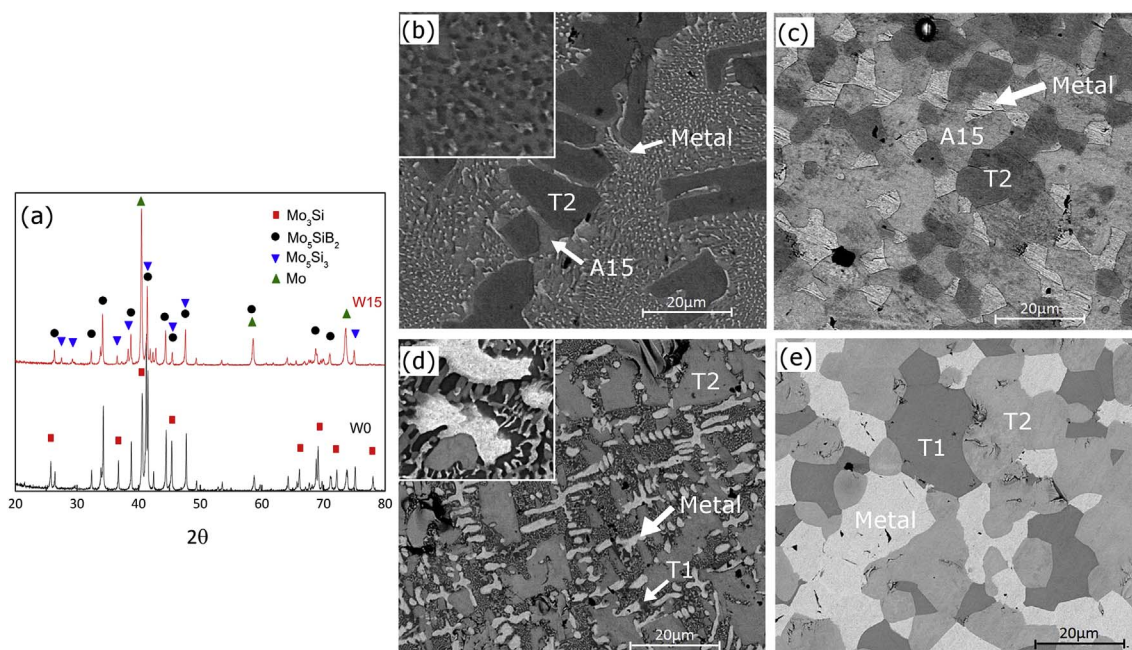


Fig. 1. Phase analysis of drop-cast and sintered alloys. (a) XRD pattern from sintered W0 and W15 alloys; (b) drop-cast W0 alloy; (c) W0 sintered alloy; (d) W15 drop-cast alloy and (e) W15 sintered alloy.

results in the formation of Nb_2O_5 . The Nb_2O_5 adheres to the surface and is highly porous, providing a continuous path for oxygen. This results in a deterioration of oxidation resistance, with significantly higher metal recession rates than Mo-Si-B alloys [16]. While the oxidation behavior of Mo-W-Si-B alloys has not been thoroughly investigated, studies on the oxidation of WSi_2 indicate an oxidation mechanism similar to MoSi_2 [20,21] with its oxidation resistance deteriorating with increasing temperature. However, the oxidation behavior of WSi_2 improves beyond 1300 °C. At lower temperatures, WO_3 was found to remain entrapped in the silica scale. The scale discontinuity provided diffusion paths for the oxygen resulting in poor oxidation resistance. However, as the temperature increased, W oxidation leads to formation of volatile WO_3 forming a passivating glassy silicate on the surface with improved oxidation resistance [20]. Therefore, it is likely that W additions will not result in a significant deterioration in the oxidation behavior of Mo-Si-B alloys, while at the same time destabilizing the A15 phase to yield a more mechanically resilient alloy.

The oxidation kinetics of Mo-Si-B alloys has been shown to be a strong function of the microstructural length scale [11], with finer microstructure showing improved oxidation resistance in comparison to coarser microstructure. Finer microstructural length scales were seen to result in rapid surface coverage. Therefore, we expect the oxidation resistance of these alloys to be affected by a complex interplay of alloy chemistry, oxidation temperature and microstructural length scales. In this paper, we focus on the oxidation mechanism of W substituted Mo-Si-B alloy, over a range of temperature, synthesized by casting and sintering resulting in two different microstructural length scales.

2. Experimental

Mo-Si-B alloys with and without W substitutions with nominal compositions $\text{Mo}_{70}\text{Si}_{15}\text{B}_{15}$ (W0) and $\text{Mo}_{55}\text{W}_{15}\text{Si}_{15}\text{B}_{15}$ (W15) were synthesized by solid state sintering and drop-casting. The sintered samples were prepared from elemental powder mixtures of Mo, W, Si and B of 99.95%, 99.9%, 99.9%, 94–96% purity with an average particle size of $\sim 3\text{--}7\text{ }\mu\text{m}$, $\sim 0.5\text{ }\mu\text{m}$, $\sim 1\text{--}5\text{ }\mu\text{m}$, $\sim < 5\text{ }\mu\text{m}$, respectively. Powders were mixed with binder (QPAC40, polypropylene carbonate) in methyl ethyl ketone (MEK) in a high density polyethylene jar using WC milling media for 24 h at 60 rpm using roller mill (Cole-Parmer Lab

mill 8000, Vernon Hills, IL). After wet milling, the slurry was dried using rotary evaporator. The dried powder was ground and sieved (through $\sim 300\text{ }\mu\text{m}$) to form granules for dry pressing. Cylindrical pellets were dry pressed uniaxially, followed by cold isostatic pressing at 310 MPa ($\sim 45\text{ ksi}$). The binder was removed by heating the pellets to 600 °C for 2 h in flowing argon atmosphere prior to sintering. All the samples were sintered at W resistance furnace (Centorr M60, Centorr Technologies) in an atmosphere of flowing ultra-high purity argon at 1925 °C for 6 h in tantalum sample holders. The cast samples were prepared from pure elemental chips (Alfa Aesar, > 99.5% purity) by arc-melting on a water cooled copper hearth in an argon atmosphere. The buttons were re-melted a minimum of four times to ensure homogeneity. The arc-melted buttons were then drop-cast in a cylindrical Cu mold to yield rods with 10 mm diameter. The drop-cast rods were annealed in an inert atmosphere using ultra-high purity argon in a W resistance furnace at 1850 °C for 10 h. Disc shaped coupons with a thickness of 1 mm and diameter of 4 mm were sectioned from these rods by electro-discharge machining for oxidation studies.

Isothermal oxidation studies were carried out in a vertical tube furnace, with the sample suspended from a microbalance (Cahn, C2000) for monitoring the mass changes continuously. In addition to the isothermal oxidation studies, transient oxidation tests were performed for sintered and cast samples in a tube furnace at 1100 and 1400 °C using ambient air. The samples were oxidized for a pre-determined time interval, and characterized using x-ray diffraction (XRD) and scanning electron microscopy (SEM). All the SEM studies were focused on representative well-defined areas of the sample in order to track the oxidation induced microstructural changes. The XRD studies were carried out using a Philips PANalytical diffractometer equipped with a double bent graphite monochromator, $\text{Cu K}\alpha$ radiation using Bragg-Brentano geometry. The SEM studies and corresponding energy dispersive spectroscopy (EDS) analyses were carried out using a FEI Quanta-250 microscope equipped with the Oxford Aztec micro-analysis system.

3. Results and discussion

3.1. Microstructures of the W substituted Mo-Si-B alloys

Substitution of Mo with W results in the removal of A15 phase (Fig. 1a). As the A15 phase gets destabilized, the metal-rich solid solution phase and the T1 (Mo,W)₅Si₃ form instead. Fig. 1b shows the microstructure of the cast Mo-Si-B alloy. The three phases present are the metal rich phase (bright contrast), the A15 phase (gray contrast) and the T2 (Mo₅SiB₂) phase shown as dark grains. The composition under consideration lies in a region where the primary solidifying phase is the T2 phase. Following the solidification of the T2 phase, the remaining liquid solidifies as a ternary eutectic, with A15 matrix and Mo_{ss} and T2 features being present as well, as seen in the inset in Fig. 1b. Such a solidification pathway has been reported in the literature for similar composition by Nunes et al. [22]. Fig. 1c shows the micrograph of the sintered alloy, which shows a significantly coarser microstructure compared to the cast alloy. A significant amount of A15 is present, as was the case with cast alloys. Substitution of Mo with W in the cast alloy results in the microstructure seen in Fig. 1d. The metal-rich solid solution forms dendrites exhibiting a bright contrast. A15 phase was not observed in this case. The T2 (M₅SiB₂, M = Mo,W) phase exhibits a gray contrast, while the T1 (M₅Si₃) phase shows a dark contrast. EDS indicated a preferential partitioning of W in the T2 phase. The data available on the thermodynamics of borides and silicides of Mo and W supports this observation. The formation enthalpies of borides of Mo and W are quite similar [23,24]. The Mo-Si interactions, however, are stronger than the W-Si interactions [25,26]. Therefore, the partitioning is driven by increasing Mo-Si bonds at the expense of W-Si bonds. The T1 phase has a higher number of M-Si bonds. Consequently, relatively small amount of W partitions in the T1 phase, with most of the W partitioning into the solid solution and the T2 phase. A comparison of Fig. 1b and d indicates that the primary solidifying phase in the two alloys is different. We are not aware of liquidus projections in a quaternary Mo-W-Si-B system or the ternary W-Si-B system. However, the microstructures indicate that the (Mo,W) solid solution solidifies dendritically, and is the primary solidifying phase. This is followed by the solidification of the remaining liquid. The Nb-Si-B system exhibits similar phase fields as well [27]. The presence of a ternary eutectic comprising of metal, T1 and T2 has been reported in the Nb-Si-B system. This mirrors our observations as well, in Fig. 1d. However, the large difference in the melting temperatures of W and Nb is likely to cause a shift in the actual liquidus projection. Fig. 1e shows the microstructures of the sintered Mo-W-Si-B alloys. A prominent coarsening of the grain size can be observed. The significant enrichment of metal rich solid solution in comparison to the unsubstituted alloys is obvious.

3.2. Oxidation kinetics

Fig. 2a shows the oxidation kinetics as a function of W content at 1200 °C for the drop-cast alloys. As the W content increases, the mass loss increases as well. W is significantly heavier than Mo; hence, with increasing W content, the mass change increases since a greater amount of WO₃ volatilizes from the higher W content alloys. It is important to note, however, that following the initial mass loss, all the alloys reach a relatively steady state without any further significant mass loss. Fig. 2b shows the oxidation kinetics of the alloys with zero and 10 atom% W respectively at 1200 and 1300 °C. Table 1 shows the final mass loss after 20 hours of oxidation. As the oxidation temperature increases, the rate of volatilization of the volatile oxides such as (MoO₃)₃ and (WO₃)₃ increase resulting in higher mass loss [28].

Fig. 3 shows the cross-section micrographs of the coupons, with 15 atom% W, oxidized at different temperatures. As the temperature increases, a clear trend can be seen. At the lowest temperature (1100 °C), shown in Fig. 3A, the borosilicate scale is interrupted by

the presence of another oxide, which was identified as WO₃ from a combination of x-ray diffraction (which showed the presence of WO₃ peaks) and EDS, which was employed to ascertain the presence of primarily W, in addition to oxygen in this region. The oxide scale formed at this temperature is relatively thin, compared to elevated temperatures. As the oxidation temperature increases from 1100 to 1300 °C, the volume fraction of the WO₃ embedded in the borosilicate scale reduces, until it disappears at 1400 °C, as seen in Fig. 3(d) and (e). Furthermore, even as the WO₃ content decreases, the thickness of the borosilicate layer increases. These observations are in agreement with Yoon et al. [20], who reported the presence of WO₃ embedded in the borosilicate scale. This impedes the surface coverage by the glassy borosilicate scale at lower temperatures ($T \leq 1300$ °C). At temperatures higher than 1300 °C, the WO₃ is expected to volatilize, similar to MoO₃ as a trimer [28]. It has been demonstrated in a number of silica formers that the presence of clusters or channels of non-passivating oxide interrupt the surface coverage by the borosilicate scale, and the volatilization of oxides like MoO₃ and WO₃, is essential for developing a passivating scale [5,10,29–31].

In order to understand the volatilization of the various oxide species, the vapor pressures of the volatile oxides were plotted as a function of temperature. Fig. 4 shows the vapor pressures of B₂O₃, (MoO₃)₃ and (WO₃)₃ as a function of temperature. The vapor pressure of B₂O₃ was plotted using the data reported in the NIST-JANAF table [32]. The vapor pressure for (MoO₃)₃ was plotted using the values reported by Gulbransen *et al.* [33]. Like MoO₃, WO₃ volatilizes in the form of a trimer, (WO₃)₃. The vapor pressure of (WO₃)₃ has been reported over 1253–1396 °C by Gulbransen *et al.* [34]. A linear fit was obtained between logP and 1/T, and this was used to extrapolate the data over wider temperature ranges. At 1100 °C, the MoO₃ has a sufficiently high vapor pressure and volatilizes. B₂O₃ and WO₃ are not expected to volatilize at this temperature. As the oxidation temperature is increased beyond 1300 °C, the vapor pressure of (WO₃)₃ is sufficiently high to volatilize from the surface. Consequently, at elevated temperatures, in Fig. 3(d) and (e), a significant amount of WO₃ could not be observed. This figure helps in constructing the oxidation mechanism of these alloys, in part. As the oxidation temperature is increased, peeling initially starts ($T \sim 700$ °C), with the volatilization of MoO₃ in the form of (MoO₃)₃. The WO₃, however does not volatilize initially due to a low vapor pressure. The presence of WO₃ on the surface will impede the surface coverage by the borosilicate scale. As the oxidation temperature increases further, the vapor pressure of (WO₃)₃ increases ($T \sim 1300$ °C), resulting in volatilization of both (MoO₃)₃ and (WO₃)₃. Over this temperature range, the viscosity of the borosilicate scale is expected to change as well. Loss of boron, in the form of boria will result in an increase in the viscosity. However, as the temperature decreases, the viscosity of boron depleted silica decreases as well. The balance of these two factors will determine the rate of surface coverage by the borosilicate scale, and hence the oxidation resistance.

3.3. Microstructure evolution during transient oxidation

A series of transient oxidation experiments were carried out for short durations, using cast and sintered samples at 1100 and 1400 °C to establish the progression of scale formation. The surface microstructures of the cast alloys, before and after oxidation at 1100 °C for 2 min are shown in Fig. 5. Fig. 5a and b shows the backscattered electron images before and after the oxidation of the W0 alloy, while Fig. 5c and d shows the corresponding secondary images. The BSE images show a clear change in the contrast after oxidation of the W0 alloy (Fig. 5a vs b). The bright Mo lamellae disappear, as the T2 phase starts exhibiting a brighter contrast. The corresponding SE images provide information on the changes in surface topography. The Mo lamellae have been removed almost completely from the surface due to evaporation of (MoO₃)₃, resulting in the formation of pores. Similarly, a significant

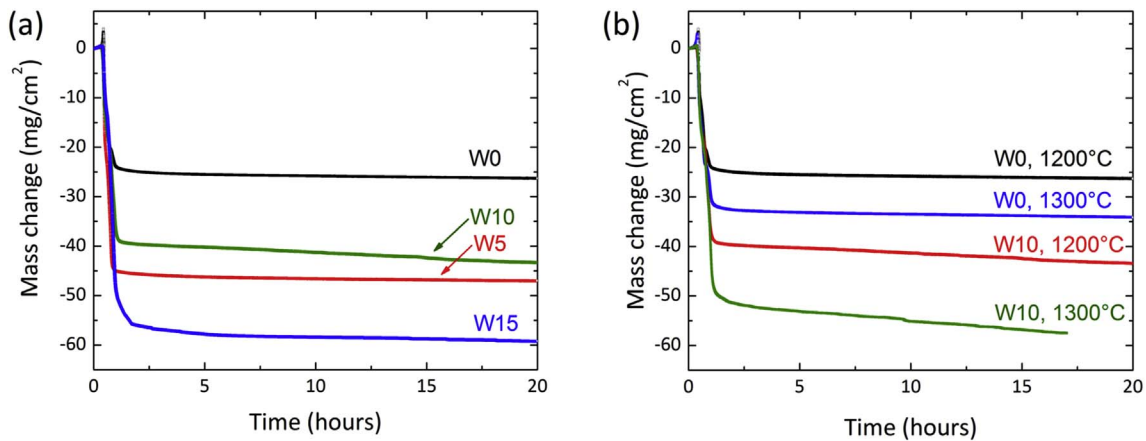


Fig. 2. . (a) Effect of composition on the oxidation kinetics at 1200 °C; (b) Effect of temperature on the oxidation kinetics of alloys with and without W.

Table 1

Final mass loss after 20 h of oxidation (the value for mass loss for W10 at 1300 °C was recorded at 17 h).

| Temperature (°C) | Mass Loss (mg/cm ²) | | | |
|------------------|---------------------------------|--------|--------|--------|
| | W0 | W5 | W10 | W15 |
| 1200 | −26.27 | −47.05 | −43.43 | −59.15 |
| 1300 | −34.12 | | −57.49 | |

amount of material appears to have been lost from T2 grains. However, lower partial pressures in the subsurface results in the formation of MoO₂, which results in the bright Z contrast seen in Fig. 5b. This is in accordance with the results published by Roy *et al.* [35]. The A15 matrix oxidizes to form (MoO₃)₃, which evaporates, and a silica layer that covers the surface. The change in surface morphology due to the volatilization is apparent in Fig. 5c and 5d. Rioult *et al.* have also reported the rapid formation of a silica layer on the A15 phase [11]. However, they also demonstrated that this layer is highly porous, and does not ultimately lead to a protective scale. The microstructural evolution is also consistent with the work of Roy *et al.*, on the transient oxidation behavior of Mo₇₆Si₁₄B₁₀ alloy at 1150 °C [36].

Fig. 5e and f shows the backscattered electron images of the W15 alloy before and after the oxidation process. Fig. 5g and h shows the corresponding secondary electron images. It can be seen that W15 exhibits significant differences in oxidation behavior and does not show surface relief similar to Fig. 5b. This is largely due to the presence of WO₃ on the surface, which, unlike the MoO₃, does not evaporate at

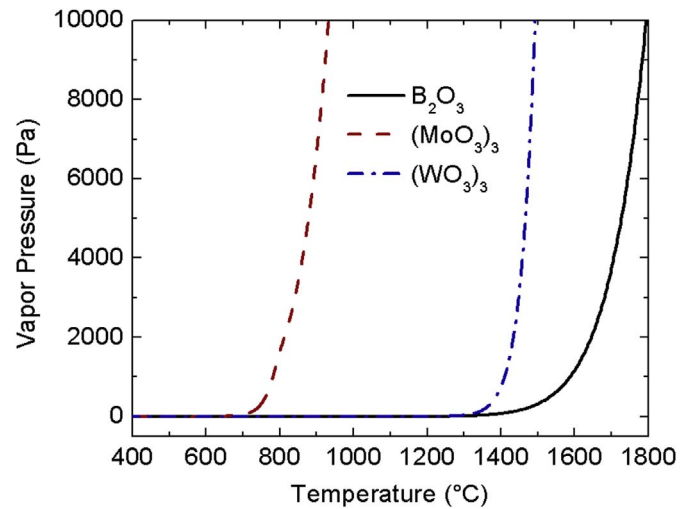


Fig. 4. Variation of vapor pressure with temperature.

1100 °C (Fig. 5f). Therefore, instead of a subsurface (Mo,W)O₂ and silica, one can observe a phase embedded in the glassy oxide on the T2 phase. Due to the limitations of the experimental technique (EDS), the amount of B could not be accurately quantified in the oxide, but the glassy oxide is likely to be a borosilicate glass. This phase was identified as WO₃, on the basis of EDS measurements, which indicated the presence of W and oxygen, and x-ray diffraction studies, which indicated the presence of WO₃. Similarly, lack of WO₃ evaporation

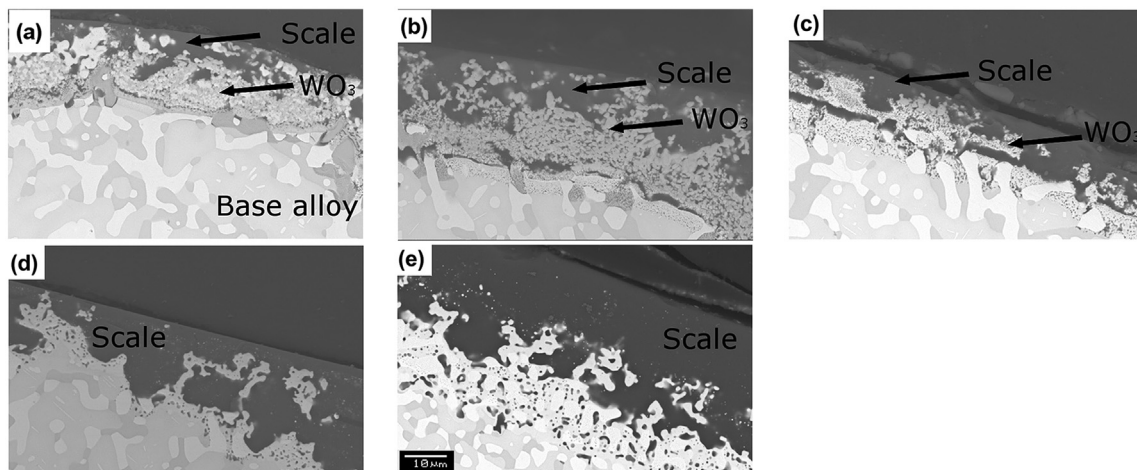


Fig. 3. Cross-section micrographs of coupons oxidized for 2 h at (a) 1100 °C, (b) 1200 °C, (c) 1300 °C, (d) 1400 °C and (e) 1500 °C.

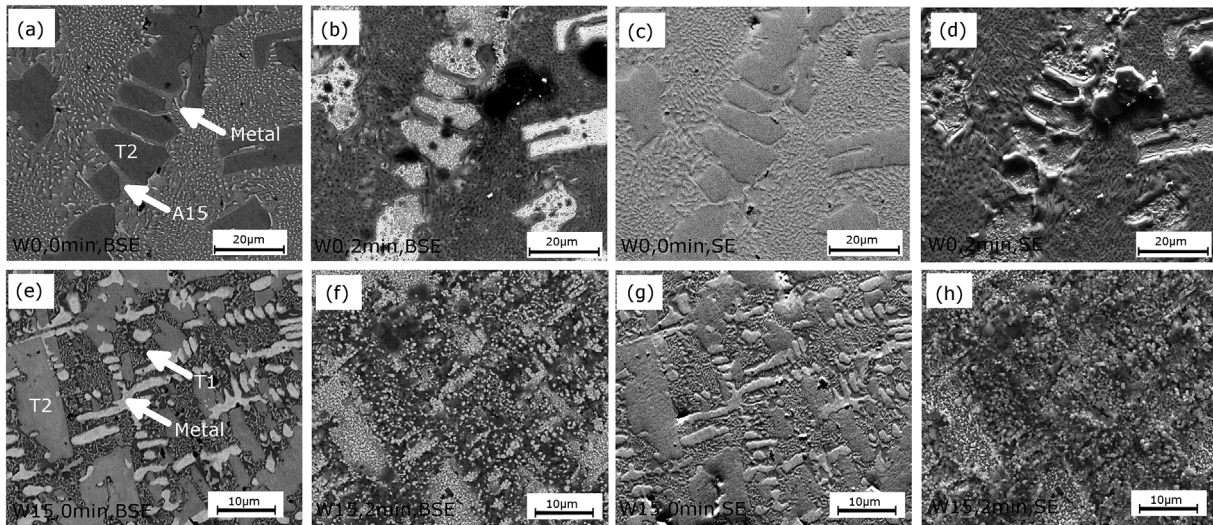


Fig. 5. (a) BSE image of the W0 surface prior to oxidation; (b) BSE image of the surface after 2 min of oxidation at 1100 °C; (c) SE image of the W0 surface prior to oxidation; (d) SE image of the surface of the surface (e) BSE image of the W15 surface prior to oxidation; (f) BSE image of the surface after 2 min of oxidation at 1100 °C; (g) SE image of the W0 surface prior to oxidation; (h) SE image of the surface after 2 min of oxidation at 1100 °C.

leads to the presence of the trioxide on the metal rich regions of the alloy. The T1 phase behaves somewhat similar to the T1 phase in the Mo-Si-B alloy studied by Meyer et al. [37]. A dense SiO_2 layer, in which the subsurface oxidation is dominated by oxygen diffusion does not form until the later stages of oxidation. During the transient stage, T1 oxidizes to form MoO_3 (and WO_3) along with SiO_2 .

3.4. Effect of microstructural length scales on oxidation

The microstructure evolution of the W15 alloys during oxidation at 1400 °C is shown in Fig. 6a–f. This can be understood by studying the topographic contrast in the secondary images. After 30 s of oxidation, these changes are fairly visible. The T1 grains, containing relatively smaller amounts of W recede faster, while the WO_3 formed during the oxidation of T2 and the (Mo,W) solid solution persist initially on the surface, imparting a “higher” topographic relief. With time, the WO_3 starts evaporating. The changes in the T2 grains are quite significant. The relatively small amount of W in T2, compared to the solid solution, coupled with higher Si and B content results in the formation of a

continuous silica rich scale as the WO_3 evaporates, and this is reflected clearly in the BSE images (grains appearing darker due to enhanced silica formation). The coarser grain structure of the sintered alloys amplifies the differences between the oxidation behaviors of the various phases (Fig. 6d–f). The T1 oxidizes to form near exclusive silica scale. Oxidation of T2 results in the formation of a silica rich scale as well, but the scale is interrupted by the presence of WO_3 . The metal rich grains are almost completely covered with WO_3 (Fig. 6e). The granular WO_3 features allow oxygen pathways to the underlying alloy. Si rich phases underneath the metal rich grains provide a supply of Si to form SiO_2 , but this can not adequately seal the surface unless the WO_3 evaporates. The WO_3 indeed does evaporate with time, as seen in Fig. 6f would show, but the rate of evaporation is much slower compared to MoO_3 due to its significantly lower vapor pressure (Fig. 4). The SiO_2 scale is responsible for the oxidation resistance of these alloys. The glassy silica layer needs to flow, especially over the metal rich regions in order to passivate the surface. Evaporation of the metal oxides abets this process. Therefore, the oxidation behavior is dominated by two factors – (a) rate at which the metal oxides form and evaporate, which is a

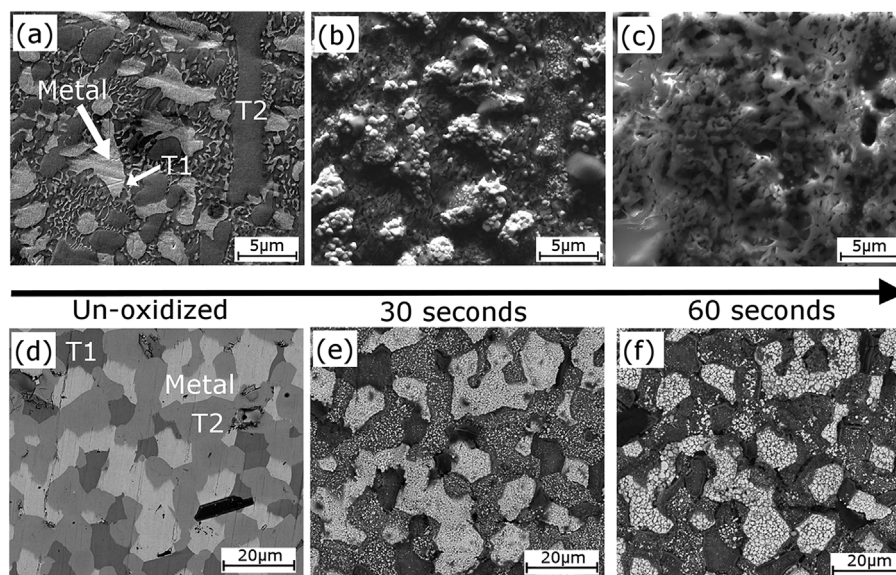


Fig. 6. Oxidized surface microstructure evolution during the oxidation of cast (a–c) and sintered (d–f) W15 alloy at 1400 °C.

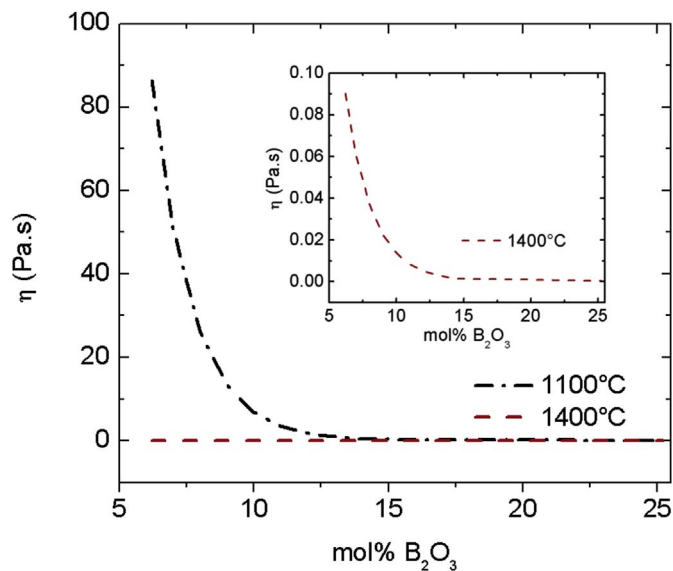
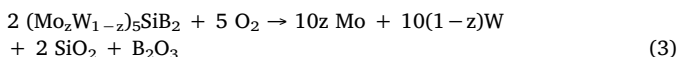
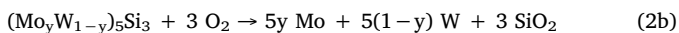
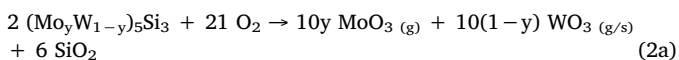
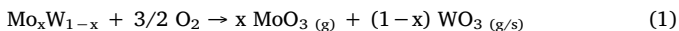


Fig. 7. Effect of B_2O_3 content on viscosity of borosilicate scale. Inset – magnified view of the viscosity at 1400 °C.

strong function of temperature and alloy chemistry, as well as (b) the length scales over which the glassy scale needs to flow in order to attain complete surface coverage.

The effect of microstructural length scales is a net balance of the rate of volatilization, which is governed by the vapor pressures of the respective oxides – $(MoO_3)_3$, $(WO_3)_3$ and B_2O_3 , as well as the resulting changes in the borosilicate scale viscosity as a function of temperature and B_2O_3 loss (which is dependent on the duration of the oxidation process). At 1100 °C, the MoO_3 has a sufficiently high vapor pressure and volatilizes. B_2O_3 and WO_3 are not expected to volatilize at this temperature. As the temperature increases to 1400 °C, all three oxides will volatilize. The evaporation rate being proportional to the vapor pressure and the molar mass, MoO_3 and B_2O_3 evaporate at a higher rate than the WO_3 , which has the highest molar mass and the lowest vapor pressure. Fig. 7 shows the variation of the viscosity of the borosilicate liquids as a function of B_2O_3 composition at 1100 and 1400 °C (inset). This figure was plotted using the data reported by Urbain et al. [38]. The viscosity increases sharply with a reduction in B_2O_3 content. Viscosity measurements by Urbain et al., for pure SiO_2 over 1653–2003 °C [38], when extrapolated to 1400 °C would result in a viscosity in excess of 2 Pa s. A comparable viscosity at 1100 °C would require the presence of 10–14% of B_2O_3 . As the temperature increases to 1400 °C, the B_2O_3 content decreases rapidly, and the viscosity of pure SiO_2 remains over 2 Pa s. Combined with the rapid rate of evaporation of $(MoO_3)_3$, a significant recession rate would be expected during the oxidation process. However, the relatively slower evaporation of $(WO_3)_3$ is expected to allow sufficient time for the silica scale to flow and seal the surface thereby reducing the metal recession.

The possible reactions during the oxidation process, following the work of Meyer & Akinc [10], and Wang et al. [39] on the oxidation behavior of Mo_5Si_3 between 800 and 1300 °C are listed below –



At temperatures below 1300 °C, WO_3 does not volatilize. Hence,

reactions (1) and (2a) result in a competition, primarily between mass losses due to volatilization of MoO_3 , and mass gain, due to the presence of stable WO_3 . Above 1300 °C, both MoO_3 and WO_3 are volatile, and hence equations (1) and (2a) result in significant mass loss, or alloy recession. From the above reactions, it becomes apparent that the overall kinetics will also be governed by the partitioning of W in the various phases. Significant W partitioning occurs in the solid solution Mo-W phase, or the Mo_5Si_3 and hence will play a significant role in the kinetics. On the other hand, W partitioning in the Mo_5Si_3 phase or the Mo_5SiB_2 phase could potentially form a Mo-W solid solution as an oxidation product, in which case, we are referred back to reaction (1).

4. Conclusions

We studied the effect of W additions on the microstructures and the evolution of the surface oxide scale of Mo-Si-B alloys prepared by solid state sintering and drop-casting at 1100 °C and 1400 °C. The Mo-Si-B alloy was found to be composed of three phases – A15, Mo_{ss} and T2. Addition of 15 atom% W resulted in the destabilization of the A15 phase, with the Mo-W-Si-B alloy being comprised of (Mo,W) solid solution, $(Mo,W)_5Si_3$ T1 phase and the $(Mo,W)_5SiB_2$ T2 phase. Removal of the brittle A15 phase is a key benefit of the W substitution. The synthesis technique had a significant effect on the alloy microstructure. Sintered alloys showed larger grains, while drop-cast alloys comprised of dendritic structures and fine eutectic lamellae exhibited a relatively finer microstructure. The surface coverage by a glassy scale was influenced by the presence of refractory metal oxides on the surface. While $(MoO_3)_3$ volatilized at 1100 and 1400 °C, $(WO_3)_3$ volatilized at 1400 °C, but not at 1100 °C. Consequently, the formation of a protective scale is facilitated in W containing alloys at 1400 °C, but not at 1100 °C. The microstructures of the alloys were also found to influence the oxidation behavior significantly. Finer length scales were more amenable to faster surface coverage by the oxide scale as opposed to coarse-grained material, which is in agreement with the work of Rioult et al. [11] on Mo-Si-B alloys, without any W additions. Finer length scales were favored in terms of scale coverage for W containing alloys as well. However, the presence of WO_3 at 1100 °C impedes coverage of the surface by the glassy borosilicate. Absence of WO_3 at 1400 °C removed this impediment, and the effect of length scale on the oxidation behavior was even more pronounced. Thus, the oxidation behavior of the W substituted alloy improved with an increase in temperature. Therefore, we conclude that these alloys show a significant microstructure and temperature dependence during the transient stages of oxidation. It is perhaps advisable to pretreat these alloys at relatively high temperatures to form a protective glassy layer before use.

Acknowledgements

The authors would like to acknowledge the funding support from AFOSR HTAM under contract # FA9550-11-1-201.

References

- [1] P.K. Ray, Y.Y. Ye, M. Akinc, M.J. Kramer, Effect of Nb and W substitutions on the stability of the A15 Mo_3Si phase, *J. Alloys Compd.* 537 (2012) 65–70.
- [2] J. Nicholls, Advances in coating design for high-performance gas turbines, *MRS Bull.* 28 (09) (2003) 659–670.
- [3] J.H. Perepezko, The hotter the engine, the better, *Science* 326 (5956) (2009) 1068–1069.
- [4] M. Meyer, M. Kramer, M. Akinc, Boron-doped molybdenum silicides, *Adv. Mater.* 8 (1) (1996) 85–88.
- [5] M. Akinc, M.K. Meyer, M.J. Kramer, A.J. Thom, J.J. Huebsch, B. Cook, Boron-doped molybdenum silicides for structural applications, *Mater. Sci. Eng. A* 261 (1) (1999) 16–23.
- [6] D. Dimiduk, J. Perepezko, Mo-Si-B alloys: developing a revolutionary turbine-engine material, *MRS Bull.* 28 (9) (2003) 639–645.
- [7] J.H. Schneibel, M.J. Kramer, D.S. Easton, A Mo-Si-B intermetallic alloy with a continuous α -Mo matrix, *Scr. Mater.* 46 (3) (2002) 217–221.
- [8] J. Kruzic, J. Schneibel, R. Ritchie, Fracture and fatigue resistance of Mo-Si-B alloys

- for ultrahigh-temperature structural applications, *Scr. Mater.* 50 (4) (2004) 459–464.
- [9] M. Meyer, M. Kramer, M. Akinca, Compressive creep behavior of Mo_5Si_3 with the addition of boron, *Intermetallics* 4 (4) (1996) 273–281.
 - [10] M.K. Meyer, M. Akinc, Oxidation behavior of boron-modified Mo_5Si_3 at 800°–1300° C, *J. Am. Ceram. Soc.* 79 (4) (1996) 938–944.
 - [11] F.A. Rioult, S.D. Imhoff, R. Sakidja, J.H. Perepezko, Transient oxidation of Mo–Si–B alloys: effect of the microstructure size scale, *Acta Mater.* 57 (15) (2009) 4600–4613.
 - [12] I. Rosales, J. Schneibel, Stoichiometry and mechanical properties of Mo_3Si , *Intermetallics* 8 (8) (2000) 885–889.
 - [13] P.K. Ray, M. Akinc, M.J. Kramer, Applications of an extended Miedema's model for ternary alloys, *J. Alloys Compd.* 489 (2) (2010) 357–361.
 - [14] T. Geng, C. Li, X. Zhao, H. Xu, Z. Du, C. Guo, Thermodynamic assessment of the Nb–Si–Mo system, *Calphad* 34 (3) (2010) 363–376.
 - [15] T. Sossaman, R. Sakidja, J.H. Perepezko, Influence of minor Fe addition on the oxidation performance of Mo–Si–B alloys, *Scr. Mater.* 67 (11) (2012) 891–894.
 - [16] V. Behrani, A.J. Thom, M.J. Kramer, M. Akinc, Microstructure and oxidation behavior of Nb–Mo–Si–B alloys, *Intermetallics* 14 (1) (2006) 24–32.
 - [17] Y. Liu, A.J. Thom, M.J. Kramer, M. Akinc, Processing and Oxidation Behavior of Nb–Si–B Intermetallics, IA (US), Ames Laboratory, Ames, 2004.
 - [18] J. Cheng, S. Yi, J.S. Park, Oxidation behaviors of Nb–Si–B ternary alloys at 1100° C under ambient atmosphere, *Intermetallics* 23 (2012) 12–19.
 - [19] B.I. Portillio, S.K. Varma, Oxidation behavior of Nb–20Mo–15Si–25Cr and Nb–20Mo–15Si–25Cr–5B alloys, *Metall. Mater. Trans. A* 43 (1) (2012) 147–154.
 - [20] J.-K. Yoon, K.-W. Lee, S.-J. Chung, I.-J. Shon, J.-M. Doh, G.-H. Kim, Growth kinetics and oxidation behavior of WSi_2 coating formed by chemical vapor deposition of Si on W substrate, *J. Alloys Compd.* 420 (1–2) (2006) 199–206.
 - [21] H.-S. Kim, J.-K. Yoon, G.-H. Kim, J.-M. Doh, S.-I. Kwun, K.-T. Hong, Growth behavior and microstructure of oxide scales grown on WSi_2 coating, *Intermetallics* 16 (3) (2008) 360–372.
 - [22] C.A. Nunes, R. Sakidja, Z. Dong, J.H. Perepezko, Liquidus projection for the Mo-rich portion of the Mo–Si–B ternary system, *Intermetallics* 8 (4) (2000) 327–337.
 - [23] E.S. Domalski, G.T. Armstrong, Heats of Formation of Metallic Borides by Fluorine Bomb Calorimetry, Wright-Patterson Air Force Base, 1964.
 - [24] Q. Li, D. Zhou, W. Zheng, Y. Ma, C. Chen, Global structural optimization of tungsten borides, *Phys. Rev. Lett.* 110 (13) (2013) 136403.
 - [25] A.K. Niessen, F.R. de Boer, R. Boom, P.F. de Châtel, W.C.M. Mattens, A.R. Miedema, Model predictions for the enthalpy of formation of transition metal alloys II, *Calphad* 7 (1) (1983) 51–70.
 - [26] F.R. De Boer, R. Boom, W.C.M. Mattens, A.R. Miedema, A.K. Niessen, Cohesion in Metals, North Holland, Amsterdam, 1988.
 - [27] D.M.P. Júnior, C.A. Nunes, G.C. Coelho, F. Ferreira, Liquidus projection of the Nb–Si–B system in the Nb-rich region, *Intermetallics* 11 (3) (2003) 251–255.
 - [28] O.J. Lu-Steffes, R. Sakidja, J. Bero, J.H. Perepezko, Multicomponent coating for enhanced oxidation resistance of tungsten, *Surf. Coatings Technol.* 207 (2012) 614–619.
 - [29] M. Meyer, A. Thom, M. Akinc, Oxide scale formation and isothermal oxidation behavior of Mo–Si–B intermetallics at 600–1000°C, *Intermetallics* 7 (2) (1999) 153–162.
 - [30] G. Ouyang, P.K. Ray, M.J. Kramer, M. Akinc, Effect of AlN substitutions on the oxidation behavior of ZrB_2 –SiC composites at 1600° C, *J. Am. Ceram. Soc.* 99 (10) (2016) 3389–3397.
 - [31] G. Ouyang, P.K. Ray, M.J. Kramer, M. Akinc, High-temperature oxidation of ZrB_2 –SiC–AlN composites at 1600° C, *J. Am. Ceram. Soc.* 99 (3) (2016) 808–813.
 - [32] M.V. Chase, NIST-JANAF Thermochemical Tables, American Institute of Physics, 1998.
 - [33] E.A. Gulbransen, K.F. Andrew, F.A. Brassart, Vapor pressure of molybdenum trioxide, *J. Electrochem. Soc.* 110 (3) (1963) 242–243.
 - [34] E.A. Gulbransen, K. Andrew, F. Brassart, P. Blackburn, Oxidation of Tungsten and Tungsten Based Alloys, Westinghouse Electric Corp., Research Labs., Pittsburgh, 1961.
 - [35] B. Roy, Khushboo, J. Das, R. Mitra, S.K. Roy, Effect of oxygen partial pressure on the cyclic oxidation behavior of Mo76Si14B10, *Metall. Mater. Trans. A* 44 (7) (2013) 2910–2913.
 - [36] B. Roy, J. Das, R. Mitra, Transient stage oxidation behavior of Mo76Si14B10 alloy at 1150 °C, *Corros. Sci.* 68 (2013) 231–237.
 - [37] M.K. Meyer, A.J. Thom, M. Akinc, Oxide scale formation and isothermal oxidation behavior of Mo–Si–B intermetallics at 600–1000°C, *Intermetallics* 7 (2) (1999) 153–162.
 - [38] G. Urbain, Y. Bottinga, P. Richet, Viscosity of liquid silica, silicates and aluminosilicates, *Geochim. Cosmochim. Acta* 46 (6) (1982) 1061–1072.
 - [39] F. Wang, A. Shan, X. Dong, J. Wu, Oxidation behavior of Mo–12.5Si–25B alloy at high temperature, *J. Alloys Compd.* 459 (1–2) (2008) 362–368.